

# Computational Analysis of Vortex Structures Induced by a Synthetic Jet to Control Separated Flows

Koichi Okada,\* Taku Nonomura,<sup>1</sup> Kozo Fujii,<sup>1</sup> and Koji Miyaji<sup>2</sup>

\*Department of Ocean and Space Engineering, Division of Systems Integration, Graduate School of Engineering, Yokohama National University, Yokohama, Kanagawa, Japan  
Currently, Engineering Solution Division, Ryoyu Systems Co., Ltd., Nagoya, Aichi, Japan  
okada@flab.isas.jaxa.jp

<sup>1</sup>Department of Space Flight Systems, Institute of Space and Astronautical Science, Japan Aerospace Exploration Agency, Sagami-hara, Kanagawa, Japan  
{nonomura, fujii}@flab.isas.jaxa.jp

<sup>2</sup>Division of Systems Research, Faculty of Engineering, Yokohama National University, Yokohama, Kanagawa, Japan  
miyaji@ynu.ac.jp

[Received date 4/12/2012; Accepted date 9/24/2012]

## ABSTRACT

The vortex structure of a separated flow over a backward-facing step controlled by a synthetic jet is investigated by using an implicit large-eddy simulation with a high-order compact difference scheme. The computation results show that mixing in the shear layer is not enhanced, when the flow is controlled at the normalized frequency of 2.0 based on the height of backward-facing step. In this case the separation length is similar to that in the case without flow control because weak and short periodic vortices are induced by the synthetic jet, and they weakly interact with the shear layer and diffuse in the recirculation region. On the other hand, the separation length becomes 20% shorter when the flow is controlled at  $F_h^+ = 0.2$  than that in the case without flow control. Strong two-dimensional vortices generated from the synthetic jet interact with the shear layer, which increases the periodic component of the Reynolds stress within that layer. These vortices are deformed into three-dimensional structures, which strengthen the nonperiodic component of the Reynolds stress in the recirculation region.

## 1. INTRODUCTION

Flow separation appears in various applications in the fields of aeronautical and mechanical engineering, and it has negative impacts on the performance of those applications. Therefore, the control of the separated flow has been continuously and extensively investigated. Recently, active flow control using microscale devices has received significant attention. One such flow control device is a “synthetic jet” [1], which consists of an orifice connected to a cavity, whose bottom oscillates at a small amplitude and produces a weak, periodic flow from the orifice. It has been reported that flow separation over an airfoil can be controlled by a synthetic jet, which induces a weak and periodic flow from its orifice exit. An advantage of using a synthetic jet over conventional flow control devices is its active flow-control capability. Other advantages of synthetic jets include their light weight and compactness and the fact that they do not require a pneumatic supply. Therefore, synthetic jets are considered suitable for a wide range of aircrafts, especially unmanned air vehicles, microscale air vehicles, and rotorcraft.

However, the practical applications of synthetic jets have been limited to the control of low-speed flows because of its relatively small output power. To control the high Mach-and-Reynolds-number and high-dynamic-pressure flow with synthetic jets, it is necessary to understand the flow-control mechanism of the jets and redesign the mechanism using a physics-based model instead of the current trial-and-error experimental studies. Although it is important to understand the characteristics of a flow induced by a synthetic jet device, these characteristics have not been clarified yet.

Most of the experiments on synthetic jets have demonstrated the effects of the synthetic jet on flow control or have discussed the optimal conditions to operate the synthetic jet around an airfoil or a

backward-facing-step configuration. Amitay et al. [2], Amitay and Glezer [3], Glezer et al. [4], and Seifert and Darabi [5] have analyzed the effects of several parameters in their experiments, as well as the effects of the installation position, nondimensional jet frequency (based on the chord or separation lengths and freestream velocity), and jet mass flow on flow-separation control around an airfoil. Previous studies have shown that actuation with both the nondimensional jet frequencies of  $O(1)$  and  $O(10)$  (based on the airfoil chord length) works satisfactorily, whereas the actuation with the nondimensional jet frequency of  $O(10)$  works better.

In addition, several computational studies have been conducted. You and Moin [6] performed LES of flow separation over an airfoil using a synthetic jet. They showed that the key mechanism in flow-separation control is the modification of the boundary-layer profile by adding or removing the directional momentum of the flow to or from the boundary layer, in addition to the enhancement of the mixing. Dandois et al. [7] conducted DNS and LES of the flow over a rounded ramp using a synthetic jet. They compared the low-frequency ( $F^+ = 0.5$ ) and high-frequency ( $F^+ = 4.0$ ) excitations and concluded that low-frequency excitation works best because turbulent kinetic energy is satisfactorily produced in this case. Okada et al. [8, 9] conducted computational simulations of a synthetic jet in a quiescent state and showed the importance of flow within a cavity; they recommended the inclusion of an internal cavity for the numerical simulation. Moreover, they illustrated the effects of Reynolds and Strouhal numbers of a synthetic jet on the generated zero-net-mass jet flow in a quiescent state.

Moreover, there are a lot of studies for flow control using other devices. Chun and Sung [10] have experimentally investigated flow-separation control in a backward-facing-step configuration using local forcing, whereas the turbulent inflow is imposed. They concluded that an  $F^+_{\theta}$  (based on the momentum thickness of the shear layer and freestream velocity, whose definition is different from that of the flow around an airfoil) of 0.01 works better. This frequency is near the frequency of the natural-vortex shedding of an unforced flow. Wengle et al. [11] conducted experiments and direct numerical simulations (DNS) of transitional flow-separation control over a backward-facing step by blowing/suction excitation with an initially laminar flow. They concluded that the optimum frequency corresponds to an  $F^+_{\theta}$  of 0.012, whose laminar-to-turbulent transition is the most amplified. In addition, Yoshioka et al. [12, 13] experimentally studied the separation control of a backward-facing-step configuration using periodic excitation. They showed that actuation with a nondimensional frequency  $F^+_h$  (based on the height of the backward-facing step and freestream velocity, whose definition is different from that of the flow around an airfoil) of 0.2 works best. Dejoan and Leschziner [14] performed large eddy simulations (LES) of the flow experiments over a backward-facing step, conducted by Yoshioka et al. Dejoan and Leschziner's computation reproduces the flow features obtained in the experiments, and they concluded that a flapping motion can be observed when flow is excited at the optimum frequency,  $F^+_h$  of 0.2.

Although previous studies have mainly shown the efficiency of flow-separation control with a synthetic jet and other devices, the mechanism of separation control has not been discussed in greater detail. In this study, the flow fields of a synthetic jet, used for flow-separation control, are analyzed to understand the mechanics of flow-separation control by a synthetic jet. Separated flow fields around a backward-facing step with and without a synthetic jet are computationally simulated, and the change in massively separated flow by the synthetic jet is discussed. A backward-facing-step configuration is selected for this study because of the fixed separation point and simpler flow field and geometry than those around an airfoil; therefore, we have a smaller number of parameters for the flow and geometric conditions. While previous studies have shown the frequency effect of a synthetic jet on the separation control, there are two different opinions on the optimum frequency ( $F^+ = 1$  or  $F^+ = 10$ ) for the separation control. This analysis focuses on the frequency characteristics of a synthetic jet controlling the separated flow.

## 2. EXPERIMENTAL SETTINGS

### 2.1. Configuration of the Synthetic Jet

A synthetic jet with a geometric configuration shown in Ref. [15] is selected for use in this study (Fig. 1). The nondimensional orifice depth,  $d$ , is equal to the nondimensional orifice width,  $b$ . The cavity depth,  $Z_D$ , is  $5d$ , and the cavity width,  $X_L$ , is  $7.5d$ . The cavity-span length in the  $y$ -direction is set to be wide enough for the simulation; therefore, a two-dimensional configuration is adopted in this study.

The oscillation of the cavity wall is defined by Eq. (1) as follows:

$$h_w(x, t) = A \cdot \sin(2\pi F^+_h t) \quad (1)$$

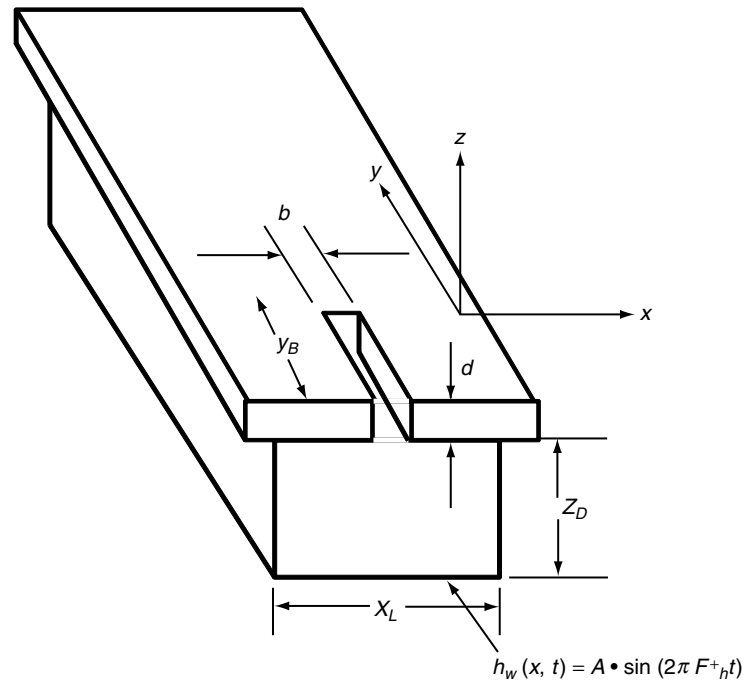


Figure 1. Current synthetic-jet configuration.

Here the amplitude of the wall's oscillation,  $A$ , is a constant.  $F_h^+$  is the nondimensional frequency of the wall's oscillation. The input parameters are shown in the Section 2.3, which describes flow conditions.

## 2.2. Configuration of Backward-Facing Step

The backward-facing-step configuration and flow conditions are the same as those of Jovic's study [16] because this experiment has comparable data to validate the case without the synthetic jet control. Figure 2 shows the backward-facing-step configuration. All the dimensions in the figure are in centimeters, but the figure is not to scale. Areas colored in gray show the computational regions in this study.

The synthetic jet is located near the edge of the backward-facing step because a previous study [2] reported the optimal location for a synthetic jet is near the separation point (the edge of the backward-facing step). The cavity of the synthetic jet is located between  $-0.5 h$  and  $-0.125 h$  from the edge of the backward-facing step. (See Fig. 4)

## 2.3. Flow Conditions

The inlet flow Mach number and Reynolds number, based on the height of the backward-facing step and the freestream velocity, are 0.2 and 5000, respectively. Here a 99% boundary layer thickness is  $1.2 h$  at  $x/h = -3.15$ . The inflow boundary layer is turbulent. The Reynolds number and the boundary layer thickness are the same as those in Jovic's study [16]. A synthetic jet has two important input parameters that are commonly used for describing the operating conditions for flow control: nondimensional frequency and momentum coefficient. The nondimensional frequency denotes the wall-oscillation frequency of the synthetic jet, and the nondimensional momentum coefficient denotes the ratio of the momentum of the synthetic jet and freestream.

$$F_h^+ = fh/u_\infty, \quad C_\mu = w_{j\max}^2 d/u_\infty^2 h \quad (2)$$

where  $f$ ,  $h$ ,  $u_\infty$ , and  $w_{j\max}$ , are the dimensional frequency of the wall's oscillation, height of the backward-facing step, freestream velocity, and temporally maximum value for the spatially averaged orifice exit velocity, respectively. In this study, three cases are analyzed: Synthetic-jet-off (without a



### 3. COMPUTATIONAL APPROACH

#### 3.1. Numerical Methods

Three-dimensional, compressible Navier–Stokes equations nondimensionalized by freestream sound speed, density, and reference length are employed as the governing equations. These equations are solved in the generalized, curvilinear coordinates by the in-house code LANS3D [17] (which represents “LU-ADI Navier–Stokes code for three-dimensional flows”), developed at ISAS/JAXA. This code is based on an efficient and accurate method for analyzing complicated flow fields by solving compressible Navier–Stokes equations. The spatial derivatives of convective and viscous terms, metrics, and Jacobian are evaluated by a sixth-order compact-difference scheme [18], and the weak flow induced by the synthetic jet and turbulent boundary layer are resolved effectively. Near the boundary, second-order explicit difference schemes are used. Tenth-order filtering [19] with a filtering coefficient of 0.45 is applied once every time step. The spilt form of the governing equation by Visbal and Gaitonde to compute the deforming and moving meshes is used for preserving the freestream [20, 21]. For time integration, an alternating direction implicit and symmetric Gauss–Seidel (ADI–SGS) [22, 23] algorithm is used. This algorithm uses the same basic concept as that of a four-factored symmetric Gauss–Seidel (FF–SGS) [24] algorithm, which adopts the concepts of both a lower–upper symmetric alternating direction implicit (LU–ADI) [17] algorithm and a lower–upper symmetric Gauss–Seidel (LU–SGS) [25] algorithm. To ensure time accuracy, a backward second-order difference formula is used for time integration, in which three sub-iterations are adopted. The computational time step is 0.003 in nondimensional time, so the maximum Courant–Friedrichs–Lewy number becomes approximately equal to 2.0. In the standard LES approach, explicit subgrid-scale models are employed, but in an ILES approach, they are not employed. Instead, a high-order low-pass filter selectively damps poorly resolved high-frequency waves. DNS is not used because the computational resources are insufficient, and an analysis of the vortex structure that can be resolved using LES is sufficient to understand the flow-control mechanism. Turbulent inflow boundary conditions are generated by using the rescaling method by Urbin et al. [26]. The rescaling domain is  $-12.0 < x/h < -2.0$ . Outflow boundaries are located away from the edge of the backward-facing step by stretching the mesh in the streamwise direction. At the outflow boundary, all variables are extrapolated. On the lower surface, no-slip conditions are adopted along with a zero normal pressure gradient. The upper surface is treated as a slip wall ( $w = 0$ ), and the normal derivative of other variables is set to zero. A periodic boundary condition is applied to the spanwise boundaries.

#### 3.2. Computational Grids

Figure 3 shows a side view of the backward-facing step. The square region is the resolved region shown in Fig. 2. The length of the computational region of zone 1 in the streamwise direction ( $x$ -direction) is  $12h$ , and the rescaling domain is set to  $-12.0 < x/h < -2.0$ . A buffer region is configured, as shown in Fig. 3, to avoid the nonphysical reflection of acoustic waves [27]. The orifice and cavity configuration of the synthetic jet is shown in Fig. 4. The length of the computational region in the span direction ( $y$ -direction) is  $4h$ , as shown in Fig. 5. A patched-grid approach is employed to generate grids for cavity, orifice, and backward-facing step regions, as shown in Figs. 3, 4, and 5. The synthetic-jet-off case does not include the cavity and orifice regions. The grid-deformation approach, developed by Melville et al. [28], is used to generate a time-varying fluid grid system for the cavity regions, as shown in Figs. 4 and 5. This algebraic method can maintain the grid quality of the initial grid near the deforming surfaces under arbitrary, moderate deflections and rotations. The total number of grid points is approximately 7,000,000. (See Table 2) The spatial resolution of a sixth-order compact difference scheme is generally much finer than that of a conventional low-order upwind scheme. Our observation indicates that the results obtained with this method correspond to those obtained from a conventional scheme with 50–100 times more grid points [29, 30 and 31]. Between each region, 12 grid points are overlapped to maintain the same accuracy

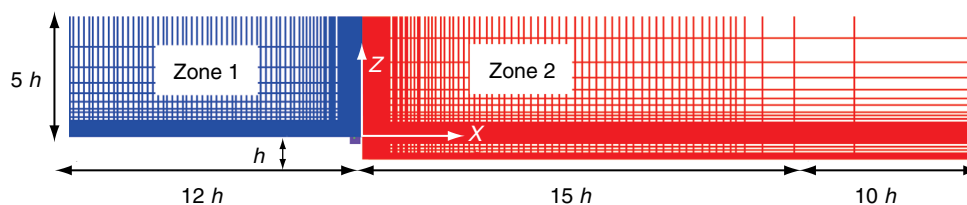


Figure 3. Computational region.

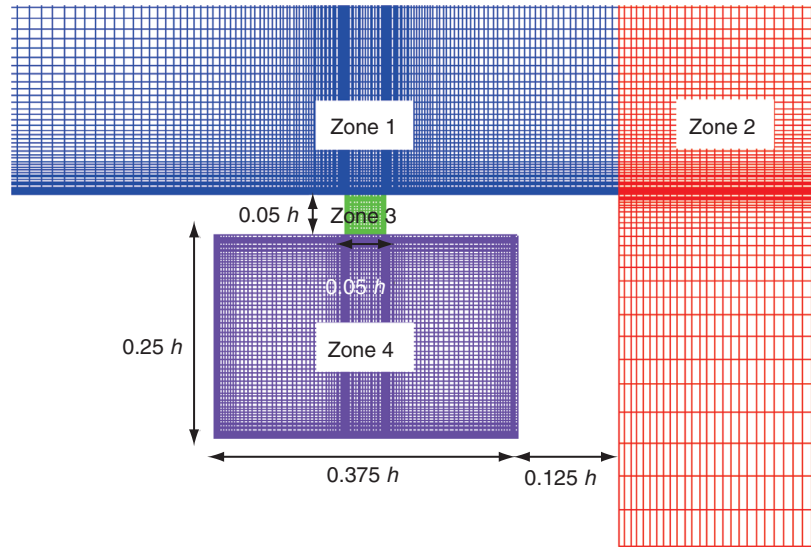


Figure 4. Cavity grid.

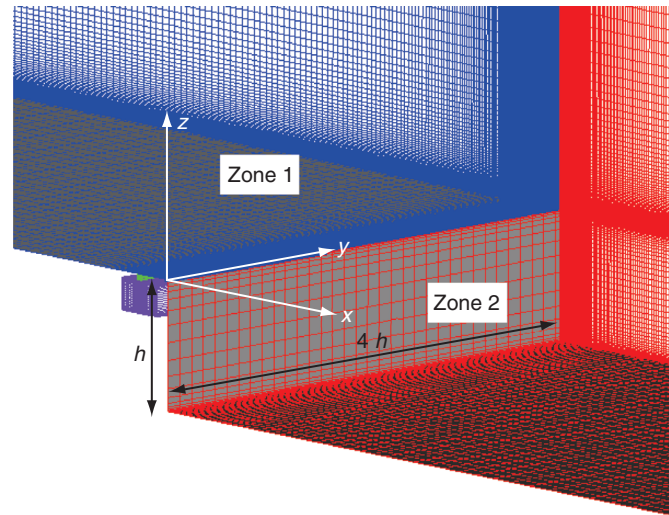


Figure 5. Computational grid.

Table 2. Number of grid points of current computational grids

Zone	Name	$j \times k \times l$	$x/h$	$y/h$	$z/h$
zone 1	backstep	$349 \times 101 \times 85$	0.0017	0.04	0.0017
zone 2	backstep	$268 \times 101 \times 138$	0.0027	0.04	0.0017
zone 3	orifice	$21 \times 101 \times 43$	0.0017	0.04	0.0017
zone 4	cavity	$99 \times 101 \times 65$	0.0017	0.04	0.0017

as that of the internal grid points in an overlapped region. The minimum grid size in each direction of all the grids is  $\Delta x = 0.0017$ ,  $\Delta y = 0.04$ , and  $\Delta z = 0.0017$ , respectively. The grid sizes in the wall units ( $\Delta x^+$ ,  $\Delta y^+$ ,  $\Delta z^+$ ) are (4, 5, 0.2) in zone 1, respectively. These values are sufficient for resolving a turbulent boundary layer. The grid points, minimum grid spacing, and computational region are set on the basis of the results of a study by Le et al. [32]. A grid-sensitivity analysis is also performed in our preliminary study.

### 3.3. Validation

The simulation results for synthetic-jet-off are compared with those of Jovic's experiment [16] to validate the grid resolution and numerical methods. The simulation results for synthetic-jet-off are

discussed in detail in a previously published paper [33]. The inflow Mach number is less than 0.2, different from that for Jovic's experiment. A Mach number in this range apparently does not strongly affect the computational results, and a Mach number of 0.2 is selected to increase the computational efficiency. The time-and-spanwise-averaged skin friction coefficients are compared in Fig. 6. The computational results agree well with the experimental results. Table 3 shows the reattachment point of the experimental and computational results. The reattachment point is the location at which the skin friction is zero; it also agrees with those of the experimental results. Figure 7 shows time-and-spanwise-

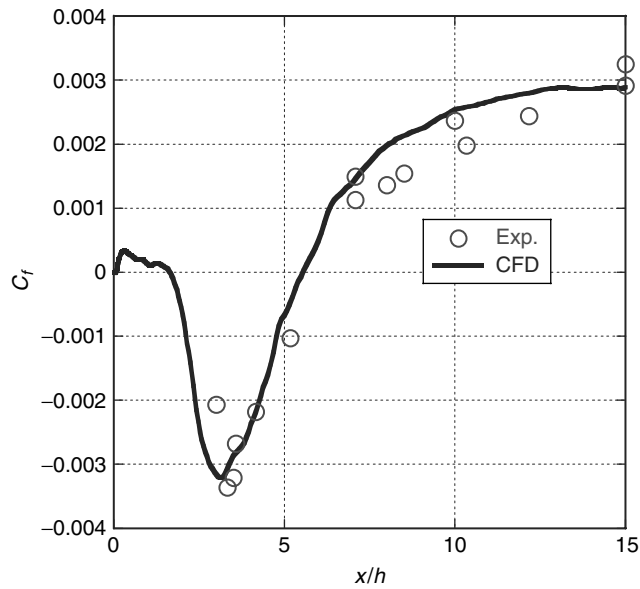


Figure 6. Skin friction coefficient for the synthetic-jet-off case compared with experimental data.

Table 3. Reattachment location

Case	Reattachment location
Exp.	6.0h(+/-0.15 h)
CFD	5.85 h

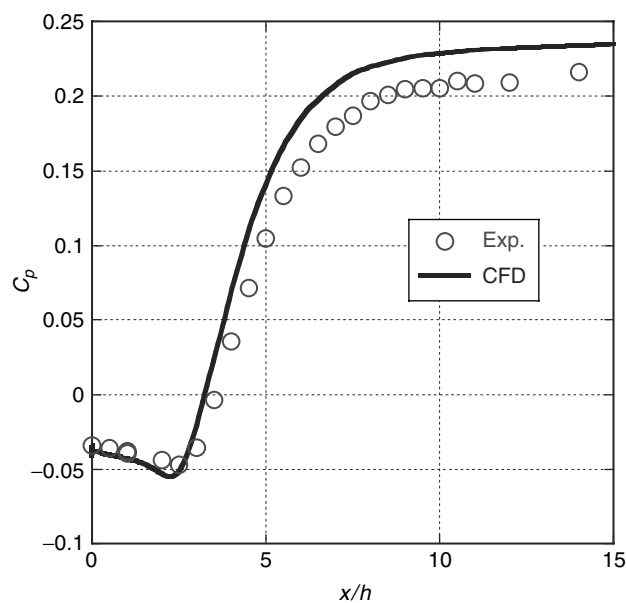


Figure 7. Pressure coefficient for the synthetic-jet-off case compared with experimental data.

averaged pressure coefficients compared with Jovic's results. These computational results agree well with the experimental results from  $x/h = 0.0$  to  $3.0$ , but they show a slightly higher value from  $x/h = 4$  to  $10$ . This might be because of gradual stretching of the grid in the flow direction at zone 2, as shown in Fig. 3, although the DNS computational result by Le et al. [32] also shows the same trend. These numerical errors in the time-averaged skin friction and pressure coefficients are sufficiently small for a qualitative understanding of the frequency characteristics of the synthetic jet and flow field. The simulation results for synthetic-jet-off agree well with the experimental results, and in addition, the applicability of the computational code with respect to various flows have been well examined in Refs. [29, 30 and 31].

## 4. RESULTS AND DISCUSSIONS

### 4.1. Time-averaged Flow Fields

Figure 8 shows the time-and-spanwise-averaged skin-friction coefficient on the bottom wall ( $0.0 < x/h < 10.0$ ) for each case. The distance from the edge to the reattachment position for  $F_h^+ = 0.2$  is evidently shorter than that for the synthetic-jet-off and  $F_h^+ = 2.0$ . Table 4, which lists the recirculation length computed from the skin-friction coefficient, shows that the length of the separation region of  $F_h^+ = 2.0$  is similar to that for the synthetic-jet-off, whereas the length of the separation region of  $F_h^+ = 0.2$  is 20% shorter than that for the synthetic-jet-off. Figure 9 shows the time-and-spanwise-averaged Reynolds stress distribution for each case. In case of the synthetic-jet-off, strong Reynolds stress regions exist between the shear-layer ( $0.0 < x/h < 2.0$ ) and the recirculation ( $2.0 < x/h < 6.0$ ) regions. The Reynolds stress distribution for  $F_h^+ = 2.0$  is similar to that for the synthetic-jet-off; however, the

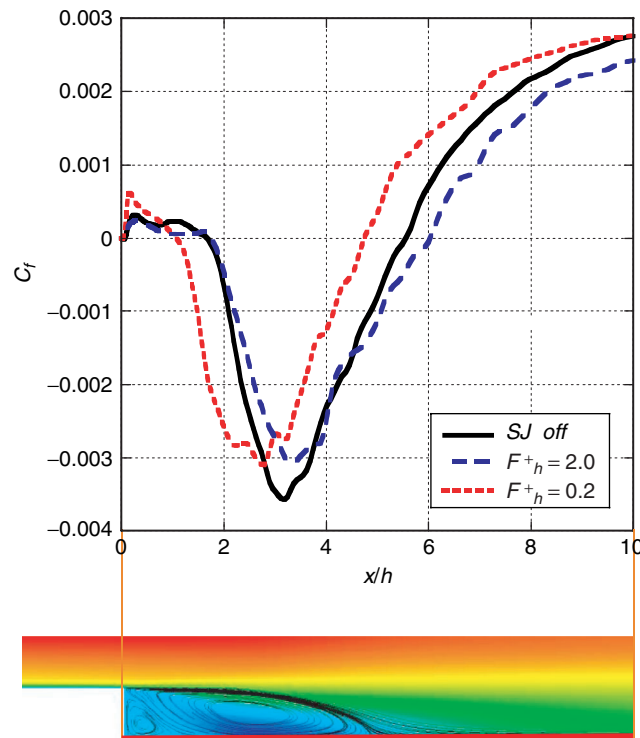


Figure 8. Skin friction coefficients of the cases examined.

Table 4. Reattachment location

Case	Reattachment location
Synthetic-jet-off	$5.85 h$
$F_h^+ = 2.0$	$6.0 h$
$F_h^+ = 0.2$	$4.75 h$

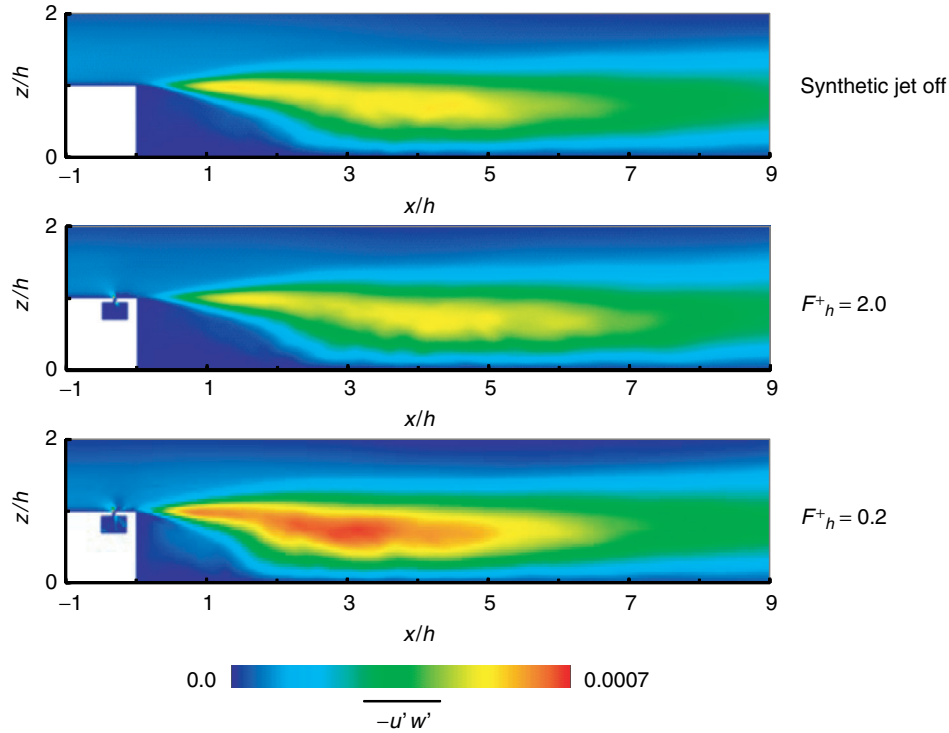


Figure 9. Reynolds-stress distribution.

Reynolds stress is slightly weaker than that for the synthetic-jet-off. On the other hand, a strong-Reynolds-stress distribution is observed at both the shear layer ( $0.0 < x/h < 1.5$ ) and the recirculation ( $1.5 < x/h < 5.0$ ) regions when  $F_h^+ = 0.2$ . Such a strong-Reynolds-stress distribution enhances the mixing of the shear layer and the recirculation regions, and the flow is quickly reattached. The shear-layer evolution along the flow is analyzed by estimating the vorticity thickness. Here, the vorticity thickness is defined as follows:

$$\delta_\omega(x) = \frac{u_\infty - u_{\min}(x)}{\max_{[z]} \left( \frac{\partial \bar{u}(x, z)}{\partial z} \right)} \quad (4)$$

Figure 10 shows the vorticity thickness of the shear layer. Vorticity thickness is usually used as a reference for the scale of thickness of the mixed and shear layers. In total, the vorticity thickness for  $F_h^+ = 0.2$  is larger than that for other cases. The Reynolds stress distribution increases at  $x/h = 1.5$  (Fig. 9). On the other hand, when  $F_h^+ = 2.0$ , the vorticity thickness is similar to that for the synthetic-jet-off and is slightly smaller in the recirculation region ( $4.0 < x/h < 6.0$ ). These time-averaged flow-fields illustrate that the Reynolds stress, vorticity thickness, mixing and reattachment point have a strong correlation; therefore, the Reynolds stress is apparently an important index of reattachment points.

#### 4.2. Spectral Analysis

Spectral analysis is conducted to understand the quantitative frequency characteristics of the flow field and vortex structure. Figure 11 shows the location of the measured spectrum points from Stations 1 to 8. These locations are along the time-averaged streamline (i.e., the shear layer) of the synthetic-jet-off. Each spectrum is averaged over 12 points in the spanwise direction. Figures 12, 13, and 14 show the one-third octave-band-filtered power spectrum densities of the vertical velocity for the synthetic-jet-off at  $F_h^+ = 2.0$  and  $0.2$ , respectively. The power spectrum densities are filtered by the one-third octave band, and the noise in the narrow-band spectrum data are removed. The vertical velocity is analyzed because it shows clearer frequency characteristics of the shear layer and vortices than those of pressure or density. The definition of the Strouhal number is the same as that of the nondimensional frequency of synthetic jet actuation, where  $F_h^+$  is used for the input parameter, and  $St$  is used to understand the

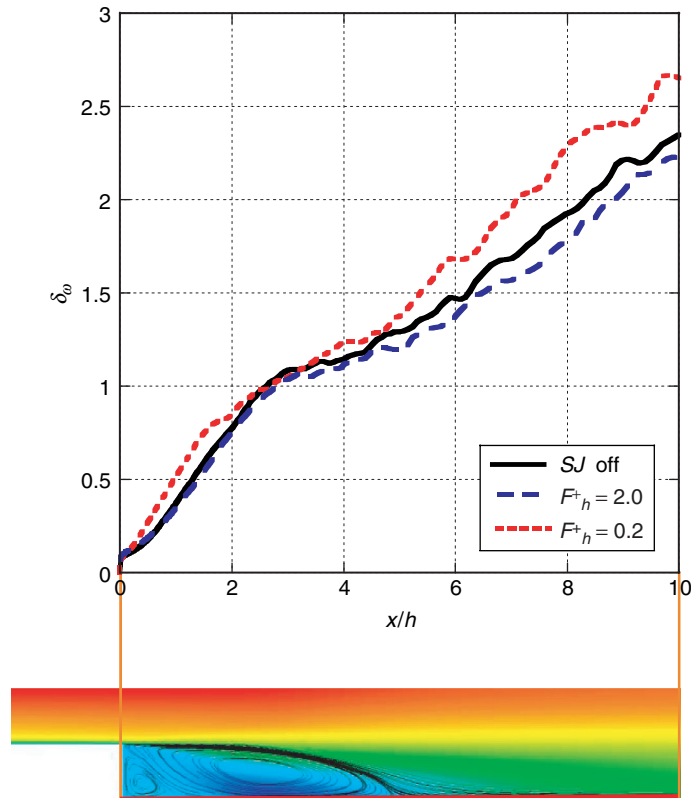


Figure 10. Vorticity-thickness evolution along the shear layer.

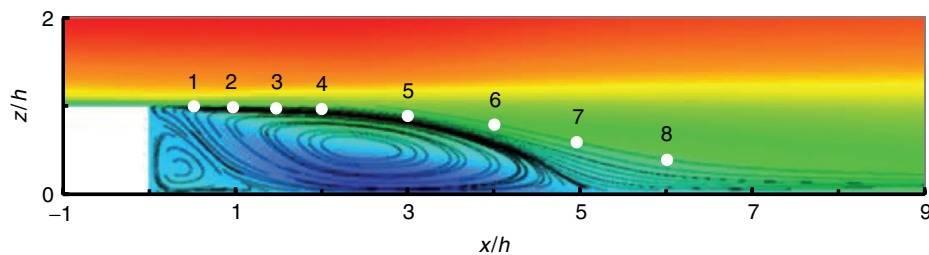


Figure 11. Location of measure points on the spectrum.

physical phenomenon. In case of synthetic-jet-off, Station 1 has a peak at  $St = 0.4$ , and its maximum value is smaller than that for other stations. Station 2 has a clear peak at  $St = 0.2$ , and the maximum value is adequate. At Station 2, the vortex pairs with the frequency of the actuation (i.e., low frequency) although its location is near Station 1. Ho and Huang [34] also discussed this pairing mechanism on the basis of an experimental study of vortex pairing in the mixing layer. At stations in the downstream region, the peak frequency decreases and the maximum value increases because the shear layer develops, as shown in Fig. 10. This corresponds to the result that the vortex scale increases further downstream (the details are described in the next section). Cases with actuation also show this trend. For  $F_h^+ = 2.0$ , the spectrum at Station 1 has a peak corresponding to the frequency actuation of the synthetic jet. This shows that vortices are generated by the actuation of the synthetic jet at  $St = 2.0$ . The level of the high-frequency component in velocity-fluctuation spectra for this case is higher than those for the other cases because the synthetic jet is actuated at a high frequency ( $F_h^+ = 2.0$ ). The peak shifts to the lower-frequency side, and the maximum value increases because the vortices of the various scales generated in the shear layer increase. The trend of the spectrum in this case is similar to that for the synthetic-jet-off case, except for the high-frequency region. For  $F_h^+ = 0.2$ , Station 1 has three clear peaks at  $St = 0.2, 0.4$ , and  $0.6$ , of which the first and second peaks are dominant. The first peak

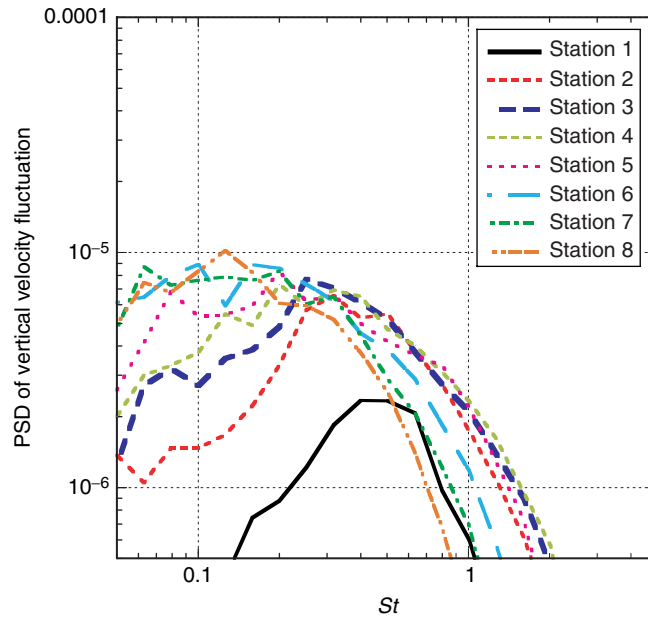


Figure 12. Filtered power-spectrum density of vertical velocity fluctuation for one-third octave band (Synthetic-jet-off).

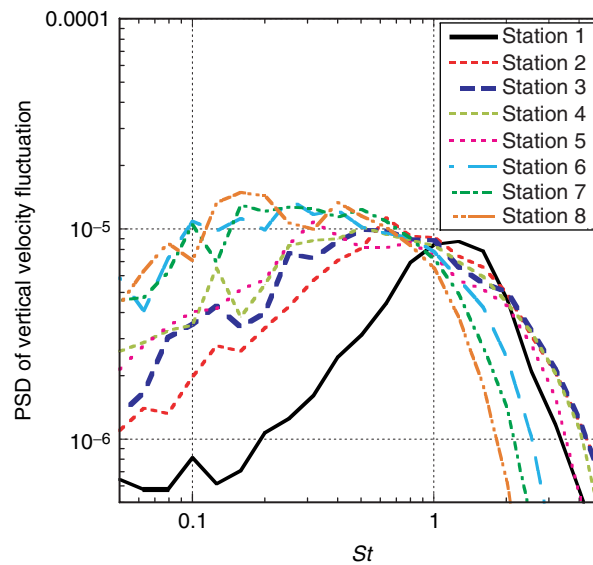


Figure 13. Filtered power-spectrum density of vertical velocity fluctuation for one-third octave band ( $F_h^+ = 2.0$ ).

corresponds to the input frequency of the synthetic jet and the vortices generated from the synthetic jet, whereas the second and third peaks correspond to the harmonic components. The second and third peaks might represent the nonlinear phenomenon of the fluid, i.e., breakup and stretching of vortices induced by the shear layer. The peak shifts to the lower-frequency side, and the maximum value increases because more vortices of various scales are generated in the shear layer. In the order Stations 3 ( $x/h = 1.5$ ), 4 ( $x/h = 2.0$ ), and 5 ( $x/h = 3.0$ ), the maximum values of the second and the third peaks decrease, whereas the maximum value of the first peak increases, and it has the maximum value because of vortex pairing at Station 3 ( $x/h = 1.5$ ), similar to the synthetic-jet-off case. Details are presented in the phase-averaged analysis discussed later. Therefore, the vorticity thickness reaches a plateau, as shown in Fig. 10. Moreover, Ho and Huang [34] show that start of the plateau agrees with

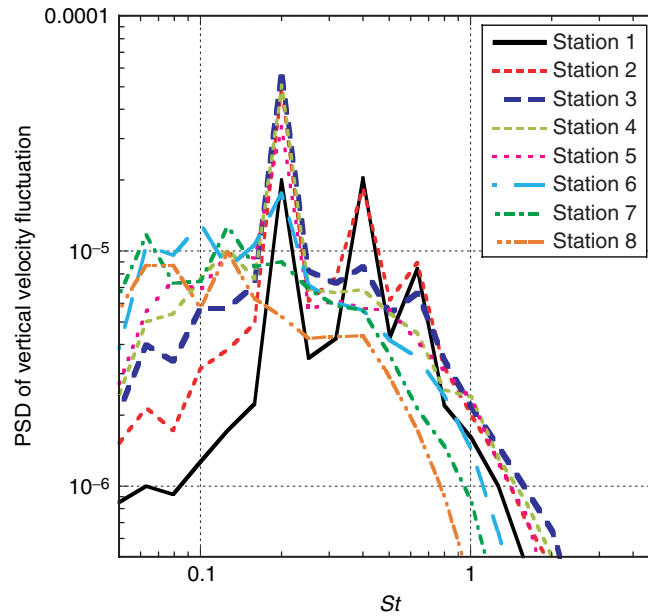


Figure 14. Filtered power-spectrum density of vertical velocity fluctuation for one-third octave band ( $F_h^+ = 0.2$ ).

the location of vortex pairing. In addition, the location of vortex pairing corresponds to the spread location of the Reynolds stress distribution. At Station 7, the first peak disappears because the vortices disintegrate, as shown in the phase-averaged analysis. Additionally, the spread Reynolds stress region corresponds to the location of vortex pairing and diffusion, as shown in Fig. 8. Morris and Foss [35] showed that the unstable frequency of the turbulent shear layer is  $St_\theta = f\theta/u_{ave} = 0.022\text{--}0.024$  from the experimental study of vortex pairing in the mixed layer, where  $\theta$  denotes the momentum thickness, and  $u_{ave}$  denotes the averaged velocity of both sides of the shear layer. In this study, the reference length is set to the height of the backward-facing step, and the unstable frequency of the turbulent shear layer approximately corresponds to  $St_h = fh/u_\infty = 0.2$ . The flow separation is suppressed when  $F_h^+ = 0.2$  because the unstable frequency is near the input frequency of the synthetic jet. Therefore, this implies that the frequency normalized by the momentum thickness of the separated shear layer (boundary layer) might be a better parameter than that normalized by the the separation length, whose optimum value is unclear in previous studies of separated flow around an airfoil [2, 3, 4 and 5], as discussed in Section 1. This optimum value based on the momentum thickness is well corresponding to that of the previous studies in which the backward-facing step is controlled using other devices. [10, 11, 12, 13 and 14]

### 4.3. Phase-averaged Analysis

A phase-averaged analysis is conducted, and the vortex structure and generation mechanisms of the Reynolds stress for  $F_h^+ = 2.0$  and  $F_h^+ = 0.2$  are investigated. This analysis is effective for analyzing periodic phenomenon in turbulent shear and mixed layers and it distinguishes between the periodic and turbulent fluid motions [36]. The frequency of phase averaging is set to be the same as that of the synthetic-jet actuation at  $F_h^+ = 2.0$  and  $F_h^+ = 0.2$ . These frequencies are the most dominant for each case, as shown in Figs. 11 and 12.

Figures 15 and 16 show the phase-and-span-averaged contour surface of static pressure and the contour lines of the second invariant of the velocity gradient tensor  $Q$  at each phase for  $F_h^+ = 2.0$  and  $F_h^+ = 0.2$ , respectively. The contour lines clearly show the vortex structures. For  $F_h^+ = 2.0$ , periodic vortices are developed near the edge of the backward-facing step, but they diffuse further downstream. The vortices from the synthetic jet have a weak effect on the flow and pressure contour. For  $F_h^+ = 0.2$ , multiple vortices are shed during one cycle. At  $\varphi = 5/4\pi$ , a vortex (SL1) is induced near the edge of the backward-facing step because of the Kelvin–Helmholtz instability. Then, SL1 develops within the shear layer. At  $\varphi = 0$ , the next vortex (SL2) is induced near the edge of the backward-facing step, also because of the Kelvin–Helmholtz instability. At  $\varphi = 1/4\pi$ , a vortex (SJ) is generated from the synthetic jet. At  $\varphi = 2/4\pi$ , the SL1 and SL2 are paired because of vortex-line instability and the deceleration by

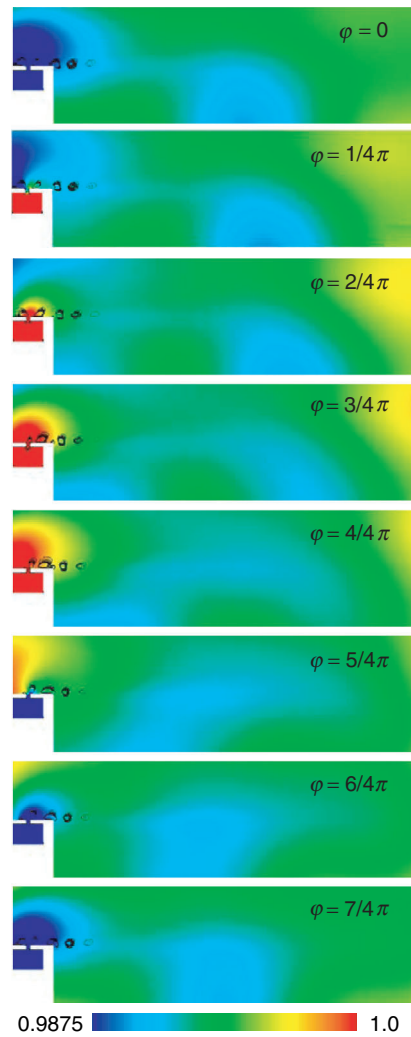


Figure 15. Phase- and span-averaged static pressure and second invariant of the velocity gradient tensor for each phase at  $F_h^+ = 2.0$  (black lines, contour range: 0.05–0.5 with 10 lines).

the adverse pressure gradient. At  $\varphi = 7/4 \pi$ , SJ and SL1 + SL2 are paired. A second pairing is observed at  $x/h = 1.5$  (Station 4), as shown in the spectrum analysis (Fig. 14), and the merged vortices are convected and diffused on the downstream side.

Figures 17 and 18 show time- and spanwise-averaged periodic (coherent) and nonperiodic (turbulent) components of the Reynolds stress distribution for  $F_h^+ = 2.0$  and 0.2, respectively. The Reynolds stress (total component) can be divided into periodic and nonperiodic components using triple decomposition. The nonperiodic component is totally dominant when  $F_h^+ = 2.0$ . The periodic component is dominant in the shear layer, whereas the nonperiodic component is dominant and especially strong from  $x/h = 1.5$  to 5.0 when  $F_h^+ = 0.2$ .

Figures 19 and 20 show the periodic and nonperiodic components of the Reynolds-stress distribution and the second invariant of the velocity gradient tensor,  $Q$ , at each phase in  $F_h^+ = 0.2$ . These data are spatially averaged in the span direction. The contour of the second invariant of  $Q$  shows the two-dimensional coherent structure of a developing vortex. The developing vortices induce the periodic component from  $x/h = 0.0$  to  $1.5 h$ . On the other hand, a nonperiodic component is induced in between vortices, and this component is especially strong in the recirculation region. This trend in Reynolds-stress distribution is similar to that of the turbulent free-shear layer [36], where the longitudinal vortices (named rib structure) [37] between two-dimensional vortices (named roller structure) [38] generate the nonperiodic component of Reynolds stress [36]. Therefore, the flow for  $F_h^+ = 0.2$  appears to have

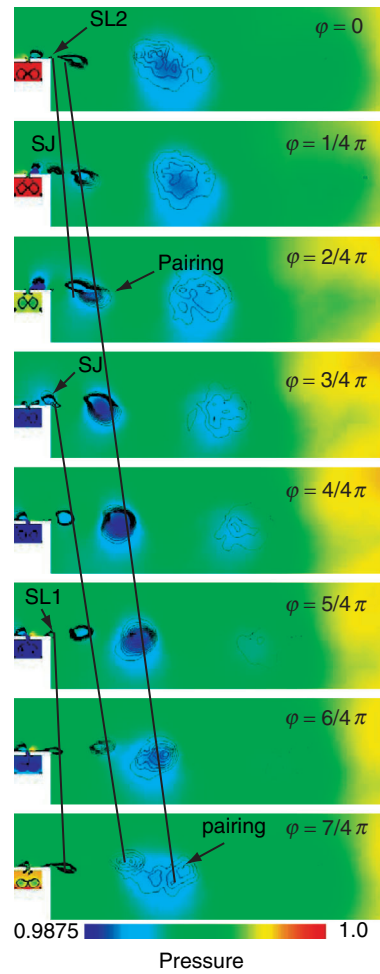


Figure 16. Phase- and span-averaged static pressure and second invariant of the velocity gradient tensor for each phases at  $F_h^+ = 0.2$  (black lines, contour range: 0.05–0.5 with 10

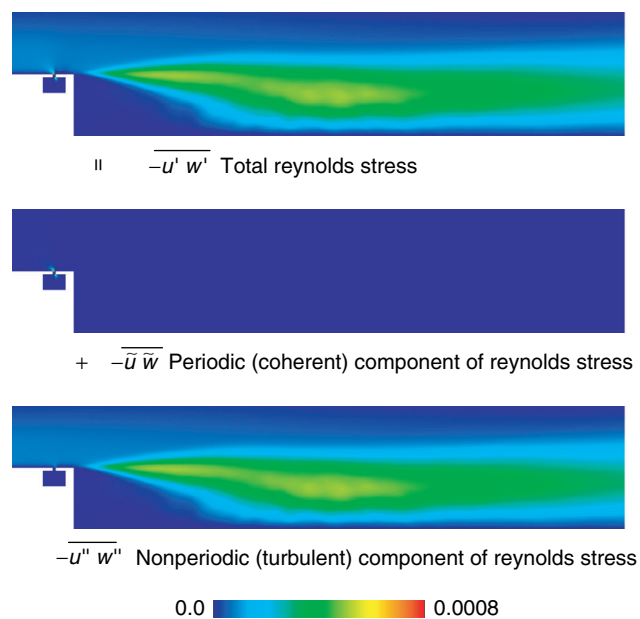


Figure 17. Time- and span-averaged total component, periodic component, and nonperiodic component of Reynolds-stress distributions at  $F_h^+ = 2.0$ .

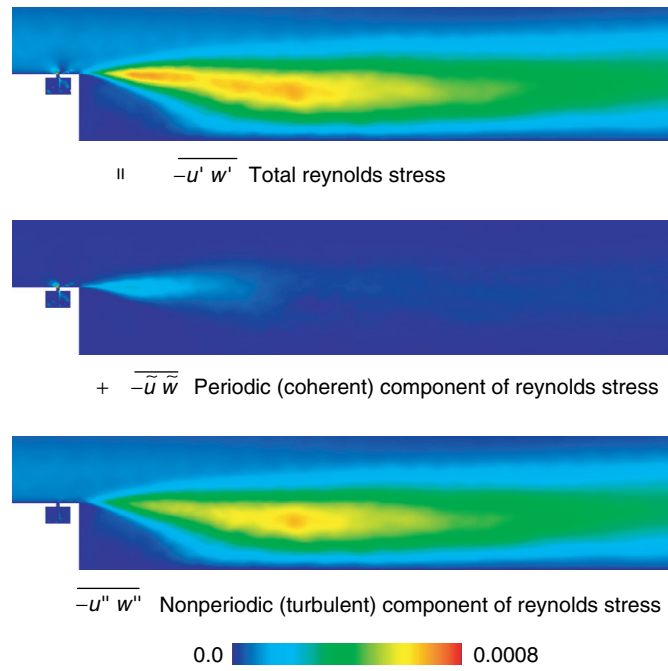


Figure 18. Time- and span-averaged total component, periodic component and nonperiodic component of Reynolds-stress distributions at  $F_h^+ = 0.2$ .

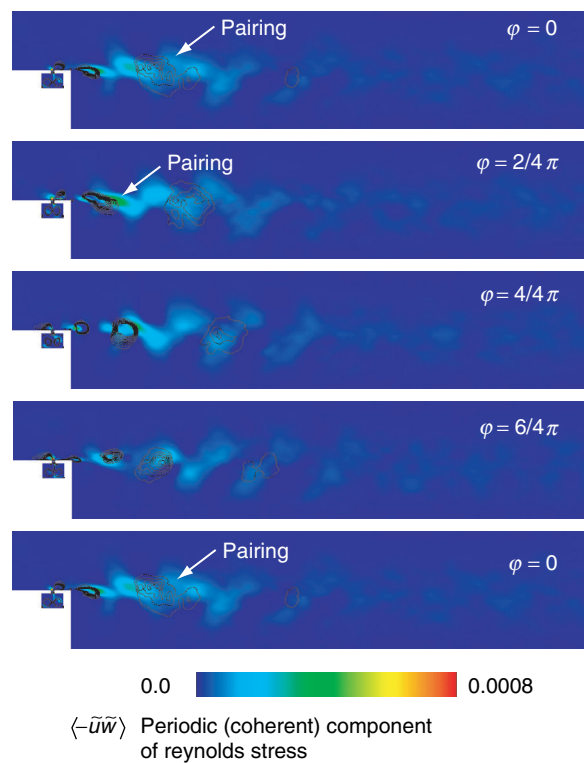


Figure 19. Phase- and span-averaged periodic component of Reynolds-stress distributions and second invariant of the velocity gradient tensor at the each phase at  $F_h^+ = 0.2$  (black lines, contour range: 0.05–0.5 with 10 lines).

flow-field characteristics similar to that of the free-shear layer, and actuation at  $F_h^+ = 0.2$  might promote these characteristics by generating two-dimensional vortices that lead to vortex pairing and turbulent

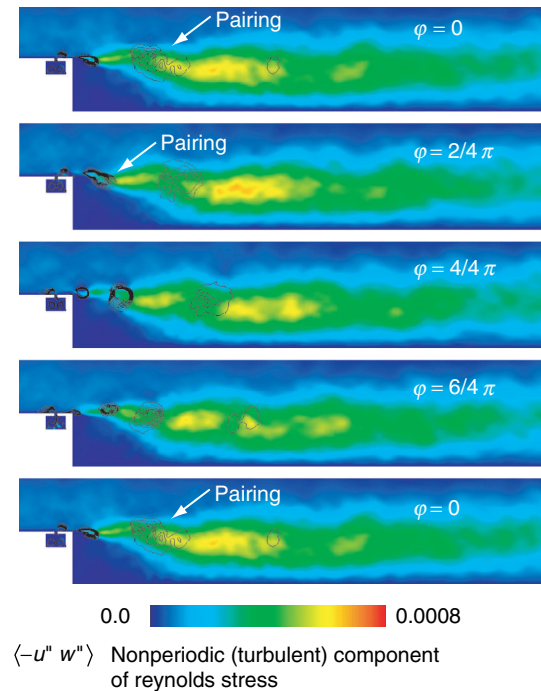


Figure 20. Phase- and span-averaged nonperiodic component of Reynolds-stress distributions and second invariant of the velocity gradient tensor at the each phase at  $F_h^+ = 0.2$  (black lines, contour range: 0.05–0.5 with 10 lines).

mixing between vortices. These flow characteristics (vortex pairing and turbulent mixing behavior) are similar to that of previous studies in which the backward-facing step is controlled by other devices with the optimum frequency actuation. [10, 11 and 14]

## 5. SUMMARY

The effect of using a synthetic jet to control the flow in a backward-facing step configuration was computationally studied, and the control mechanism of a massively separated flow was discussed. The flow fields and the effect of nondimensional frequency were investigated.

Two actuations were selected; that is, the flow with a synthetic-jet control at  $F_h^+ = 2.0$  and  $F_h^+ = 0.2$ , where the nondimensional frequency  $F_h^+$  was normalized with the height of the backward-facing step and the freestream velocity. These values corresponded to  $F^+ \sim 10$  and 1, respectively. Here the non-dimensional frequency  $F^+$  was normalized using the length of the separation region and the freestream velocity.

A time-averaged flow field showed that the separation-length size for the flow controlled by  $F_h^+ = 2.0$  is similar to the case without flow control. On the other hand, the separation length for the flow controlled by  $F_h^+ = 0.2$  was 20% shorter than that of the case without flow control. This is because a strong Reynolds stress enhances mixing in the shear layer and the recirculation region. The time-averaged flow-fields showed that the Reynolds stress, mixing, and reattachment point has a strong correlation and that the Reynolds stress is apparently an important index of the reattachment point.

In the synthetic-jet-off case, frequency analysis showed that the vortex scale increased further downstream because of vortex pairing and growth. For  $F_h^+ = 2.0$ , frequency analysis showed that weak, short periodic vortices, induced by the synthetic jet, does not affect the flow, and they are diffused in the recirculation region. The overall trends of the spectrum were similar to the synthetic-jet-off case, except for the high-frequency region. For  $F_h^+ = 0.2$ , frequency analysis showed that vortex pairing in the shear layer is enhanced by the synthetic jet, thereby resulting in a strong Reynolds stress and a shorter reattachment point, as discussed above.

The phase-averaged analysis for  $F_h^+ = 2.0$  showed that the short-period vortices, generated from the synthetic jet, are diffused in the shear layer and that the dominant Reynolds stress component is the nonperiodic one. On the other hand, the phase-averaged analysis for  $F_h^+ = 0.2$  case showed that the flow induced by a synthetic jet results in strong two-dimensional vortices and longitudinal vortices between

the two-dimensional vortices. These strong two-dimensional vortices generate the periodic component of the Reynolds stress in the shear layer, whereas the nonperiodic component of the Reynolds stress is generated between the two-dimensional vortices—similar to the free-shear layer. These periodic and nonperiodic components of the Reynolds stress enhance mixing in the separated shear layer and the recirculation region, respectively. The results above showed that it is important to induce two-dimensional vortices that promote vortex pairing and turbulent mixing among vortices.

Effective parameter settings to practically control the separated flow were discussed. Strong two-dimensional vortex pairing was induced because  $F_h^+ = 0.2$  is close to the most unstable frequency of the developing shear layer. This observation corresponds to that obtained in previous studies, [10, 11, 12, 13 and 14] though the other devices which generate disturbances are used for flow control in these studies. This implies that the essential mechanism of synthetic jet is almost the same as other devices which generate disturbances. A frequency analysis illustrated that the frequency should be normalized by the momentum thickness of the separated shear layer (boundary layer). Finally, for flow-separation control, the generation of two-dimensional vortices by a synthetic jet is important as this promotes vortex pairing and turbulent mixing between two-dimensional vortices. These observations could probably be applied for separated flows not only over the airfoils but also in other applications—even those using other active flow-control devices (e.g., a dielectric barrier discharge plasma actuator) [39].

### ACKNOWLEDGMENT

This study was partly supported by Grant-in-Aid for Scientific Research 20246122 and Strategic Programs for Innovative Research (SPIRE) of the High Performance Computing Initiative (HPCI). The authors wish to thank Dr. Kota Fukuda of Tokai University for his valuable comments on this research. The computations were conducted in JAXA's supercomputing system (JSS).

### NOMENCLATURE

$A$	=	nondimensional amplitude of the oscillation of the cavity wall
$b$	=	nondimensional orifice width
$c$	=	Speed of sound
$C_\mu$	=	nondimensional momentum coefficient
$d$	=	nondimensional orifice depth
$\delta_\omega$	=	vorticity thickness
$F^+$	=	nondimensional frequency based on separation region
$F_h^+$	=	nondimensional frequency based on the height of the backward-facing step
$F_\theta^+$	=	nondimensional frequency based on the momentum thickness of the shear layer
$h$	=	height of the backward-facing step
$h_w$	=	offset of the position of the cavity wall
$Mach$	=	Mach number
$Re$	=	Reynolds number
$Q$	=	Second invariant of velocity gradient tensor
$St$	=	Strouhal number. Definition is the same as that of $F_h^+$ .
$t$	=	time
$u$	=	$x$ -direction velocity
$u_j$	=	temporally maximum value of spatially averaged orifice exit velocity
$u_\infty$	=	freestream velocity
$w$	=	$z$ -direction velocity
$X_L$	=	nondimensional cavity width
$x$	=	nondimensional Cartesian coordinate in transverse direction
$y$	=	nondimensional Cartesian coordinate in spanwise direction
$y_B$	=	nondimensional orifice half span
$z$	=	nondimensional Cartesian coordinate in streamwise direction
$Z_D$	=	nondimensional cavity depth
$\Delta x$	=	computational grid spacing in the $x$ -direction
$\Delta y$	=	computational grid spacing in the $y$ -direction
$\Delta z$	=	computational grid spacing in the $z$ -direction
$\mu$	=	viscosity
$\varphi$	=	phase

$\theta$  = momentum thickness

### Superscript

- = time-averaged quantity  
 < > = phase-averaged quantity  
 ' = fluctuation  
 ~ = periodic fluctuation  
 " = nonperiodic fluctuation

### REFERENCES

- [1] Glezer, A. and Amitay, M., "Synthetic Jets," Annual Review of Fluid Mechanics, Vol. 34, (2002), pp. 503–529.
- [2] Amitay, M., Smith, D. R., Parekh, V. K. D. E. and Glezer, A., "Aerodynamic Flow Control over an Unconventional Airfoil Using Synthetic Jet Actuators," AIAA Journal, Vol. 39, No. 3, (2001), pp. 361–370.
- [3] Amitay, M. and Glezer, A., "Role of Actuation Frequency in Controlled Flow Reattachment over a Stalled Airfoil," AIAA Journal, Vol. 40, No. 2, (2002), pp. 209–216.
- [4] Seifert, A. and Darabi, A., "Delay of Airfoil Stall by Periodic Excitation," Journal of Aircraft, Vol. 33, No. 4, (1996), pp. 691–699.
- [5] Glezer, A., Amitay, M. and Honohan, A. M., "Aspect of Low-and High-Frequency Actuation for Aerodynamic Flow Control," AIAA Journal, Vol. 43, No. 7, (2005), pp. 1501–1511.
- [6] You, D. and Moin, P., "Active Control of Flow Separation over an Airfoil Using Synthetic Jets," Journal of Fluids and Structures, Vol. 24, (2008), pp. 1349–1357.
- [7] Dandois, J., Garnier, E. and Sagaut, P., "Numerical Simulation of Active Separation Control by a Synthetic Jet," Journal of Fluid Mechanics, Vol. 574, (2007), pp. 25–58.
- [8] Okada, K., Oyama, A., Fujii, K. and Miyaji, K., "Computational Study on Effect of Synthetic Jet Design Parameters," International Journal of Aerospace Engineering, Volume 2010 (2010), Article ID 364859.
- [9] Okada, K., Oyama, A., Fujii, K. and Miyaji, K., "Computational Study of Effects of Nondimensional Parameters on Synthetic Jets," Transactions of the Japan Society for Aeronautical and Space Sciences, Vol. 55, No. 1, (2012), pp. 1–11.
- [10] Chun, K. and Sung, H. "Control of turbulent separated flow over a backward-facing step by local forcing," Experiments in Fluids, Vol. 21, No. 6, (1996), pp. 417–426.
- [11] Wengle, H., Huppertz, A., Brwloff, G. and Janke, G. "The manipulated transitional backward-facing step flow: an experimental and direct numerical simulation investigation," European Journal of Mechanics-B/Fluids, Vol. 20, No. 1, (2001), pp. 25–46.
- [12] Yoshioka, S., Obi, S. and Masuda, S., "Organized Vortex Motion in Periodically Perturbed Turbulent Separated Flow over a Backward-facing Step," International Journal of Heat and Fluid Flow, Vol. 22, No. 3, (2001), pp. 301–307.
- [13] Yoshioka, S., Obi, S. and Masuda, S., "Turbulence Statistics of Periodically Perturbed Separated Flow over backward-facing step," International Journal of Heat and Fluid Flow, Vol. 22, No. 4, (2001), pp. 393–401.
- [14] Dejoan, A. and Leschziner, M. A., "Large eddy simulation of periodically perturbed separated flow over a backward-facing step," International Journal of Heat and Fluid Flow, Vol. 25, No. 4, (2004), pp. 581–592.
- [15] Rizzetta, D.P. and Visbal, R.M., "Numerical Investigation of Synthetic Jet Flowfields," AIAA Journal, Vol. 37, No. 8, (1999), pp. 919–927.
- [16] Jovic, S., "Backward-Facing Step Measurements at Low Reynolds Number,  $Re_h = 5000$ ," NASA TM -08807, (1994).
- [17] Fujii, K. and Obayashi, S., "High-resolution Upwind Scheme for Vortical-flow Simulations," Journal of Aircraft, Vol. 26, No. 12, (1989), pp. 1123–1129.
- [18] Lele, S. K., "Compact Finite Difference Scheme with Spectral-Like Resolution," Journal of Computational Physics, Vol. 103, No. 1, (1992), pp. 16–42.

- [19] Gaitonde, D. V. and Visbal, R. M., "Pade Type Higher-Order Boundary Filters for the Navier–Stokes Equations," *AIAA Journal*, Vol. 38, No. 11, (2000), pp. 2103–2112.
- [20] Visbal, M. R. and Gaitonde, D. V., "On the Use of Higher-Order Finite-Difference Schemes on Curvilinear and Deforming Meshes," *Journal of Computational Physics*, Vol. 181, No. 1, (2002), pp. 155–185.
- [21] Abe Y., Iizuka N., Nonomura T. and Fuji K., "Conservative Metric Evaluation for High-order Finite-Difference Scheme with the GCL Identities on Moving and Deforming Grids," *Journal of Computational Physics*, Vol. 232, (2013), pp. 14–21.
- [22] Iizuka, N., "Study of Mach Number Effect on the Dynamic Stability of a Blunt Re-entry Capsule," PhD thesis, The University of Tokyo, (2006).
- [23] Nishida, H. and Nonomura, T., "ADI-SGS Scheme on Ideal Magnetohydrodynamics," *Journal of Computational Physics*, Vol. 228, No. 9, (2006), pp. 3182–3188.
- [24] Fujii, K., "Efficiency Improvement of Unified Implicit Relaxation/Time Integration Algorithms," *AIAA Journal*, Vol. 37, No. 1, (1999), pp. 125–128.
- [25] Yoon, S. and Jameson, A., "Lower-Upper Symmetric-Gauss–Seidel Method for the Euler and Navier–Stokes Equations," *AIAA Journal*, Vol. 26, No. 9, (1988), pp. 1025–1026.
- [26] Urbin, G. and Knight, D., "Large-Eddy Simulation of a Supersonic Boundary Layer Using an Unstructured Grid," *AIAA Journal*, Vol. 39, No. 7, (2001), pp. 1288–1295.
- [27] Colonius, T., Lele, S. K. and Moin, P., "Boundary Condition for Direct Computation of Aerodynamics Sound Generation," *AIAA Journal*, Vol. 31, No. 9, (1993), pp. 1574–1582.
- [28] Melville, R. B., Morton, S. A. and Rizzetta, D. P., "Implementation of a Fully-Implicit, Aeroelastic Navier-Stokes Solver," *AIAA Paper*, (1997), pp. 97–2039.
- [29] Arasawa, T., Fujii, K. and Miyaji, K., "High-Order Compact Difference Scheme Applied to Double-Delta Wing Vortical Flows," *Journal of Aircraft*, Vol. 41, No. 4, (2004), pp. 953–957.
- [30] Kawai, S. and Fujii, K., "Analysis and Prediction of Thin-Airfoil Stall Phenomena Using Hybrid Turbulent Methodology," *AIAA Journal*, Vol. 43, No. 5, (2005), pp. 953–961.
- [31] Kawai, S. and Fujii, K. "Compact Scheme with Filtering for Large-Eddy Simulation of Transitional Boundary Layer," *AIAA Journal*, Vol. 46, No. 3, (2008), pp. 690–700.
- [32] Le, H., Moin, P. and Kim, J., "Direct Numerical Simulation of Turbulent Flow over a Backward-facing Step," *Journal of Fluid Mechanics*, Vol. 330, (1997), pp. 349–374.
- [33] Okada, K., Fujii, K. and Miyaji, K., "Computational Study of Frequency and Amplitude Effects on Separation Flow Control with the Synthetic Jet," *ASME 2009 International Mechanical Engineering Congress & Exposition*, (2009).
- [34] Ho, C. M. and Huang, L. S., "Subharmonics and Vortex Merging in Mixing Layers," *Journal of Fluid Mechanics*, Vol. 119, (1982), pp. 443–473.
- [35] Morris, S. C. and Foss, J. F., "Turbulent Boundary Layer to Single-stream Shear Layer: the Transition Region," *Journal of Fluid Mechanics*, Vol. 494, (2003), pp. 187–221.
- [36] Hussain, A. K. M. F., "Coherent Structures and Turbulence," *Journal of Fluid Mechanics*, Vol. 173, (1986), pp. 303–356.
- [37] Rogers, M. M. and Moser, R. D., "Direct Simulation of a Self-similar Turbulent Mixing Layer," *Physics of Fluids*, Vol. 6, Issue 2, (1994), pp. 903–923.
- [38] Brown, G. L. and Roshko, A., "Density Effect and Large Structure in Turbulent Mixing Layers," *Journal of Fluid Mechanics*, Vol. 64, (1974), pp. 775–816.
- [39] Corke, T. C., Enloe, C. L. and Wilkinson, S. P., "Dielectric Barrier Discharge Plasma Actuators for Flow Control," *Annual Review of Fluid Mechanics*, Vol. 42 (2010).

